Wave Processes at Gas-Gas Interfaces

Sigrid Andreae, Josef Ballmann, and Siegfried Müller

Abstract. We investigate the interaction of shock waves in a heavy gas with embedded light gas bubbles next to a rigid wall. Due to the highly dynamical, unsteady processes under consideration we use an adaptive FV scheme for the computations to resolve accurately all physically relevant effects. The results are validated by comparison with shock tube experiments.

1. Introduction

Most of the flow phenomena occuring in nature are not single-phase but two-phase flows. As a preparatory work to the analysis of wave processes at phase boundaries we deal with wave interaction phenomena, such as shock wave reflection and refraction of waves at gas-gas interfaces with a jump of the acoustic impedance. Haas and Sturtevant [HS87] performed shock tube experiments for those conditions which will be used for comparison. The primary objective of the present work is to provide an accurate prediction of all occurring wave phenomena with emphasis on wave interactions with material interfaces. Of particular interest is the occurrence of instabilities as, e.g., the Richtmyer-Meshkov instability.

2. Level Set

For tracking the propagating material interface between the two fluids we use the level set method proposed by Osher and Sethian in [OS88]. Herein, instead of an explicit description of the interface under consideration, a scalar field, ϕ, given in the domain is used to represent the motion of the interface where $\phi = 0$. However, we implemented the level set function following an approach of Mulder et al. [MO92] where the level set function is not a smooth but a discontinuous scalar field which is sometimes called "color-function". The "color" of the fluid controls which fluid is present and therefore which equation of state has to be used. It has to be noticed that we track the jump of the scalar field and not the zero value. Written in conservative form, the transport equation for the scalar field, ϕ, can be added to the system of conservation equations (1). The main advantage of this approach is the preservation of conservativity.

3. Governing Equations and Method of Solution

The fluid flow is modeled by the time-dependent 2D Euler equations for compressible fluids. Together with the transport equation for the scalar field, ϕ, this leads to the system of conservation equations

$$\frac{\partial}{\partial t}\int_V \vec{U}\ dV + \oint_{\partial V} \vec{F}\cdot\vec{n}\ dS = 0\,. \tag{1}$$

Here, $\vec{U} = (\varrho, \varrho\,\vec{v}, \varrho\,E, \varrho\,\phi)^{\mathrm{T}}$ is the array of the mean conserved quantities: density of mass, momentum, specific total energy and level set and $\vec{F} = (\varrho\,\vec{v}, \varrho\,\vec{v}\circ\vec{v} + p\vec{1}, \vec{v}\,(\varrho\,E + p), \varrho\phi\,\vec{v})^{\mathrm{T}}$ the array of the corresponding convective fluxes. p is the pressure and $\vec{v}$ the fluid velocity. Since the two fluids under consideration are gaseous both, there is no need to deal with the surface tension at their contact surface. The system of equations is closed by the perfect gas equations of state and physical properties for the two fluids under consideration. Their evaluation is governed by the scalar field ϕ.

The conservation equations (1) are discretized by a finite volume method. The convective fluxes are determined by solving quasi–one dimensional Riemann problems at the cell interfaces. For this purpose we employ a two-phase Roe Riemann solver designed for the coupled system of the 2D Euler equations and the evolution equation of the scalar field ϕ. For the construction of this solver we proceed similarly to [LV89] for real gases. In order to avoid non-physical expansion shocks we use Harten's entropy fix. The spatial accuracy is improved by applying a quasi one-dimensional second order ENO reconstruction. Due to the strong dynamic behavior of the considered flow problems the time integration is performed explicitly. In order to properly resolve all physical relevant phenomena, but, nevertheless, to limit the computational costs, a local grid adaptation strategy is employed. In distinction from previous work done in this area, we employ here recent multi-resolution techniques, see [Mül02].

Mulder observed in [MO92] that using formulation of ϕ as a "color-function" the pressure shows spurious oscillations at the material interface. To reduce these oscillations we use averaged pressure and energy equations in an ϵ-neighborhood near the interface.

4. Numerical Results

In the following we compare our numerical results with experiments performed by Haas and Sturtevant, [HS87]. Herein, a shock runs across an initially circular gas domain of helium or R22[1] in an air surrounding. In Table 1 the physical properties

[1] R22 is the heavy refrigerant chlorodifluromethane ($CHClF_2$).

TABLE 1. Material properties of air, helium and R22 at 293.15 K, 101.35 kPa.

fluid	u_{mol} [10^3kg/mol]	R [J/kg/K]	γ	c [m/s]
air	28.964	287.0	1.4	343.3
helium	4.003	2077.0	1.66	1007.4
R22	864.687	96.138	1.178	184.0

TABLE 2. Dimensionless initial conditions.

	post-shocked air	pre-shocked He	pre-shocked R22	pre-shocked air
ϱ	1.376	0.138	2.985	1.0
p	1.575	1.0	1.0	1.0
$\varrho\, c$	1.742	0.479	1.875	1.183
v_x, v_y	0.396 , 0.0	0.0 , 0.0	0.0 , 0.0	0.0 , 0.0

of the gases under consideration are given. The geometrical setup is the same for both problems. The length of the computational domain is 0.445 m and the height 0.0445 m. The bubble is placed at 0.4895 m and has a radius of 0.025 m. The initial mesh has 125 × 10 cells and 5 levels of refinement are used. Due to the mirror symmetry of the problem, only the upper half was computed. A shock coming from left impinges on a gas bubble. Initially, the bubble and the surrounding pre-shocked air are at rest and in thermal and mechanical equilibrium. The initial conditions for the problems discussed here are given in Table 2.

Helium Bubble in Air. In Figure 1(a) the incoming shock (marked as i) has already crossed the most left part of the bubble boundary. It is partly transmitted as a refracted shock (rr) and partly reflected as a rarefaction wave (rw). This behavior is governed by the ratio of the acoustic impedances ($\varrho\, c$), see values given in Table 2. Inside the bubble the transmitted shock runs ahead since the speed of sound in helium is higher than in air at the same temperature. The shock-front is curved due to the spherical shape of the undisturbed helium-air interface. The fore-running shock in helium arches as a thin, black line from $x = 0.039$ m to $x = 0.0315$ m where the shock just hits the interface. Outside the bubble the incident shock is visible as a straight, black, vertical line. The density jump at the helium-air interface is a thin, opaque line marked as (pb). Behind the shock, the reflected rarefaction wave appears as a dark area. Since in the very beginning of the shock bubble interaction the shock front is parallel to the material interface, all the waves travel in x-direction. Later on, the shock impinges on the interface under an increasing angle. Similar to the laws of geometrical optic the rarefaction wave is reflected under the same angle as the shock impinges on the helium surface. Since the shock inside is faster than outside, a shock wave (marked s as “ side” shock) emanates where the refracted shock meets the phase boundary. A complicated four shock configuration develops which Henderson explained in [HCP91] and called twin regular reflection refraction. In Figure 1(b) the refracted shock is just passing the most right boundary of the bubble at $x = 0.073\,\mathrm{m}$, whereas the incident shock is at $x = 0.043\,\mathrm{m}$. The acoustic impedance in the post-shocked helium is only $0.542\,\mathrm{kg/m^2/s}$ but in the pre-shocked air $1.183\,\mathrm{kg/m^2/s}$. Therefore, the air acts in the sense of a rigid but permeable boundary which makes that the reflected part of the shock wave hitting this boundary is a shock. This reflected shock (rl) focuses on the x-axis at $0.059\,\mathrm{m}$ which is visible as a small, light dot in the density gradients of Fig. 1(c) (marked by an arrow). As a result of the higher shock speed the helium near the x-axis is stronger accelerated than the air above it. Thereby, an anti-clockwise rotation of the bubble content is induced and at the symmetry axis the bubble constricts and develops a small throat. The helium volume remains rotating, splits up at the x-axis and travels circulating upstream, see Fig. 1(e).

We compared our results to photographs taken by Haas and Sturtevant, see [HS87], and found a good agreement see Figs. 3. In particular, the numerical results exhibit all waves visible in the schlieren photographs. However, since the numerical results do neither include the complete experimental setup, e.g., the support for cylindrical membrane in Fig. 3(c), nor perturbations due to the rupture of the membrane providing the sharp initial interface, the comparison can only be qualitative. Nevertheless, as indicated by the same labels as in Fig. 1 all the waves from the experiment are resolved in the computation. In particular, the topology of the bubble is excellently reproduced. Notice that the ring which was necessary to fix the bubble in the experiment must not be confused with a wave surface.

R22 Bubble in Air. In Figure 2(a) the shock has already entered the R22 region. Since the acoustic impedance of R22 is only slightly higher than the acoustic impedance for the post-shocked air, see Table 2, the incident shock (i) is mainly transmitted and only a small portion is reflected as a shock (rl). There, the transmitted and thereby refracted shock (rr) is visible as a concave curved black line extending from $x = 0.037\,\mathrm{m}$ to $x = 0.048\,\mathrm{m}$. Compared to the incident shock (i) the refracted shock (rr) is slower, because the sound speed in R22 is lower than in air. This is also the reason for the higher acceleration of the air above the bubble compared to that of the gas R22. This fact leads to a clock-wise rotation of the material in the R22 bubble later on. The outwards running shock diffracts since it is decelerated at the phase boundary, see Fig. 2(b). Between the incident shock (i) and the inside running shock (rr) develops a compression wave (cw). By the compression wave the flow direction is turned by 90° towards the symmetry axis. The front of the refracted shock bends more and more until it focuses on the x-axis at the phase boundary, see box on left side in Fig. 2(c). The shock is reflected after focusing and runs outwards, see wave (rf) in Fig. 2(d). Again the shock (rf) is traveling slower in the R22 than in the helium. When the incident shock has passed the bubble it crosses its symmetric counterpart, see Fig. 2(d) at $x = 0.06\,\mathrm{m}$. Thereby, a reflected shock (s) running upstream is induced. These two shocks (s and rf) pass across the bubble in upstream direction. The bubble migrates downstream and thereby it prolongates and rolls up its top (t). In Figure 2(e) the phase boundary represented by the zero level $\phi = 0$ is indicated by a solid, black line.

Obviously, there are growing instabilities on the top of the structure. It is assumed that these are Rayleigh-Taylor instabilities due to the shock passing across a curved phase boundary.

The comparison with the experiment is given in Fig. 4. Again, the ring from the experimental setup is visible. The wave (w) at the bottom of Fig. 4(c) is a reflection from the shock tube wall. A good agreement between the phase boundaries (pb), the incident and refracted shocks (i and rr) is visible in in Figs. 4(a) and 4(c). Note that even the compression wave (cw) is resolved. In Figures 4(b) and 4(d) the phase boundary (pb) as well as the shock (rf) – reflected from the focus of the refracted shock – match perfectly their experimental counterparts. At the left border the reflected shock (s) from the crossing of the incident shocks at the symmetry axis is visible.

5. Conclusion and Future Work

We presented numerical results of a multiscale based adaptive FV method for highly dynamical two-fluid flow problems with wave interactions at material boundaries. The comparison with experiments verifies that our solver is adequate for computing two-fluid flow problems for different perfect gases. The advanced grid refinement strategy automatically detects all appearing waves and provides a perfect resolution of those waves.

References

[HS87] Haas, J. F., Sturtevant, B.: Interaction of weak shock waves with cylindrical and spherical gas inhomogeneities. J. Fluid Mech., **181**, 41–76 (1987)

[HCP91] Henderson, L. F., Colella, P., Puckett, E. G.: On the refraction of shock waves at a slow-fast gas interface. J. Fluid Mech., **224**, 1–27 (1991)

[LV89] Liu, Y., Vinokur, M.: Nonequilibrium flow computations. I. An analysis of numerical formulations of conservation laws. J. Comp. Phys., **83**, 373–397 (1989)

[MO92] Mulder, W., Osher, S.: Computing interface motion in compressible gas dynamics. J. Comp. Phys., **100**, 209–228 (1992)

[Mül02] Müller, S.: Adaptive Multiscale Schemes for Conservation Laws, Lecture Notes on Computational Sciences and Engineering, Vol. **27**, Springer, 2002

[OS88] Osher, S., Sethian, J. A.: Fronts Propagating with Curvature-Dependent Speed: Algorithms Based on Hamilton-Jacobi Formulations. J. Comp. Phys.,**79**, 12–49 (1988)

Sigrid Andreae
MAN B&W Diesel AG, Augsburg
E-mail address: `sigrid.andreae@de.manbw.com`

Josef Ballmann (Presented by Author2)
Lehr- und Forschungsgebiet für Mechanik der RWTH Aachen
E-mail address: `ballmann@lufmech.rwth-aachen.de`

Siegfried Müller
Institut für Geometrie und Praktische Mathematik der RWTH Aachen
E-mail address: `mueller@igpm.rwth-aachen.de`

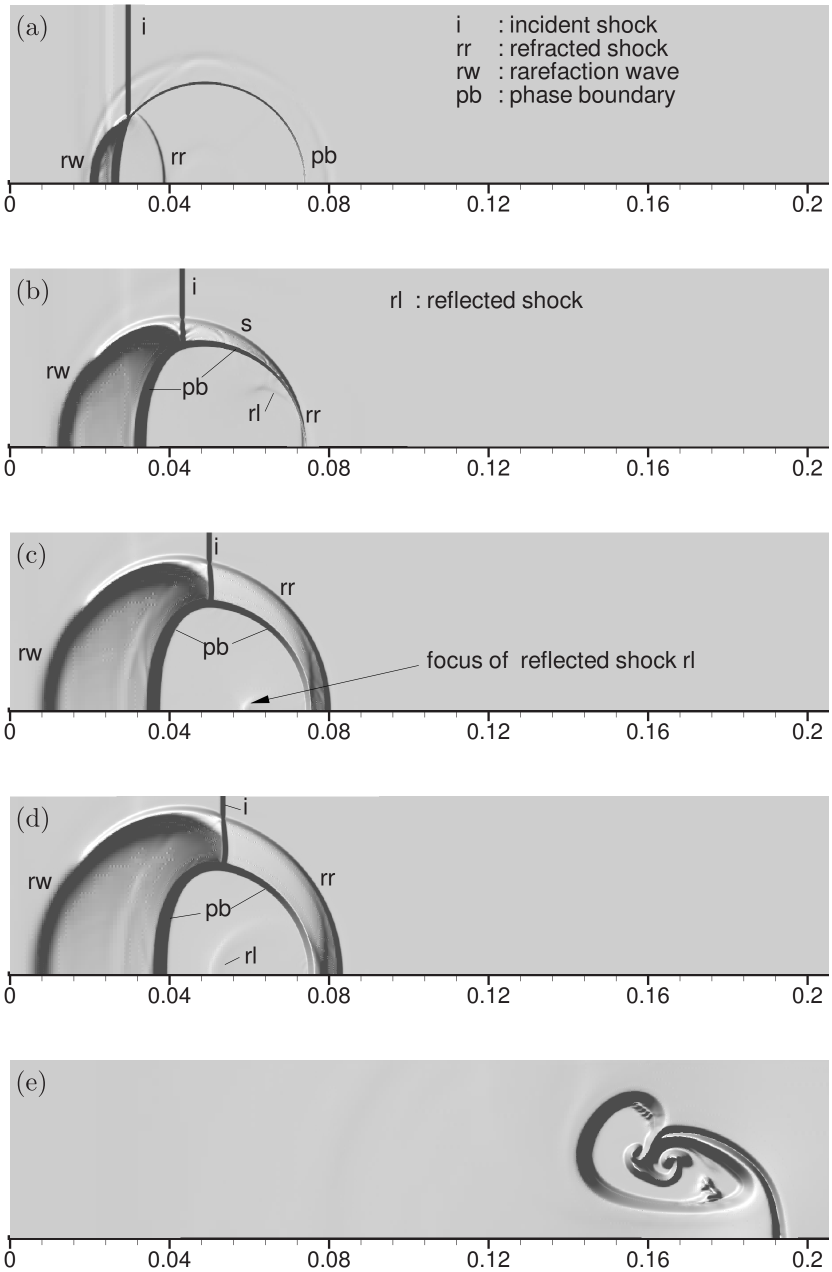

FIGURE 1. Shock-bubble (helium) interaction, (a)-(e): density gradients.

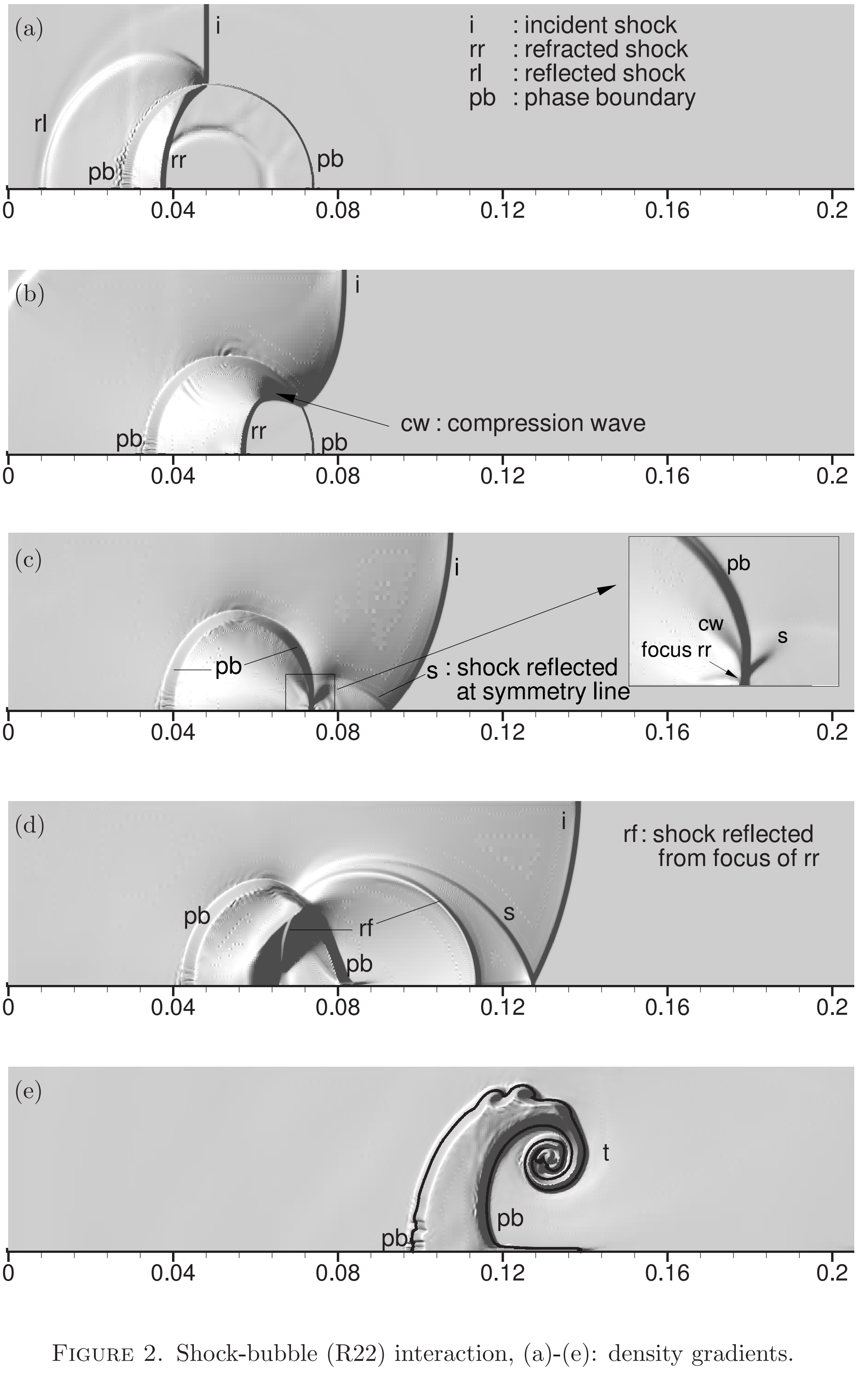

FIGURE 2. Shock-bubble (R22) interaction, (a)-(e): density gradients.

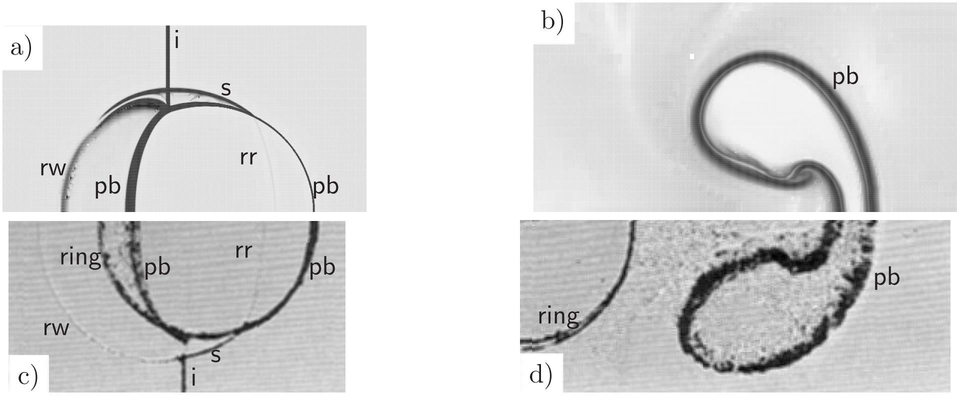

FIGURE 3. Comparison between numerical (a,b) and experimental (c,d) results for helium bubble in air. Experimental pictures scanned from [HS87]. The ring is part of the experimental setup. For the indices at the waves, see Fig. 1.

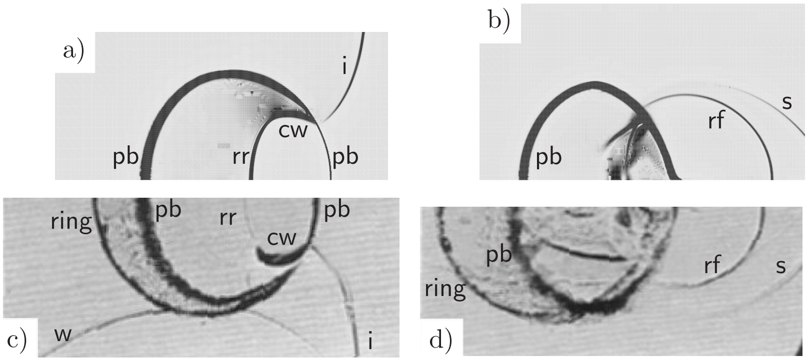

FIGURE 4. Comparison between numerical (a,b) and experimental (c,d) results for R22 bubble in air. Experimental pictures scanned from [HS87]. The ring is part of the experimental setup. For the indices at the waves, see Fig. 2.